metals

MDPI

Article

The Effect of Post-Deposition Heat Treatment on the Microstructure, Texture, and Mechanical Properties of Inconel 718 Produced by Hybrid Wire-Arc Additive Manufacturing with Inter-Pass Forging

Dmitrii Panov [1], Gleb Permyakov [2], Stanislav Naumov [1,*], Vladimir Mirontsov [3], Egor Kudryavtsev [1], Liying Sun [4,*], Alexander Aksenov [2], Nikita Stepanov [1,3], Dmitriy Trushnikov [2] and Gennady Salishchev [1]

[1] Laboratory of Bulk Nanostructured Materials, Belgorod State University, Belgorod 308015, Russia; panov_d@bsuedu.ru (D.P.); kudryavtsev@bsuedu.ru (E.K.); stepanov@bsuedu.ru (N.S.); salishchev_g@bsuedu.ru (G.S.)
[2] Department of Welding Production, Metrology and Technology of Material, Perm National Research Polytechnic University, Perm 614990, Russia; gleb.permiakov@gmail.com (G.P.); rpd@pstu.ru (A.A.); trushnikov@pstu.ru (D.T.)
[3] World-Class Research Center "Advanced Digital Technologies", State Marine Technical University, Saint-Petersburg 198095, Russia; 1580419@bsuedu.ru
[4] Institute of New Materials, Guangdong Academy of Sciences, Guangzhou 510650, China
* Correspondence: naumov_s@bsuedu.ru (S.N.); sunliying@gdinm.com (L.S.)

Abstract: The microstructure, texture, and mechanical properties of Inconel 718 fabricated via hybrid wire-arc additive manufacturing (WAAM) with inter-pass forging, and the subsequent modified post-deposition heat treatment (PDHT), were investigated. The modified PDHT included homogenization at 1185 °C and double ageing at 720 °C, with furnace-cooling to 620 °C; this process was first used for Inconel 718 obtained via WAAM and inter-pass forging. In the as-printed material, two characteristic zones were distinguished, as follows: (i) columnar grains with a preferable <100> orientation and (ii) fine grains with a random crystallographic orientation. The development of static recrystallization induced via inter-pass forging and further heating during the deposition of the next (upper) layer provoked the formation of the fine-grained zone. In the as-printed material, particles of (Nb,Ti)C and TiN, and precipitates of a Nb-rich Laves phase that caused premature cracking and failure during mechanical testing, were detected. In the PDHT material, two zones were found, as follows: (i) a zone with coarse uniaxial grains and (ii) a zone with a gradient grain size distribution. PDHT resulted in the precipitation of γ'' nanoparticles in the γ-Ni matrix and the dissolution of the brittle Laves phase. Therefore, significant hardening and strengthening, as well as increases in ductility and impact toughness, occurred.

Keywords: Inconel 718; wire-arc additive manufacturing; post-deposition heat treatment; ductility; impact toughness; strengthening

Academic Editor: Guido Di Bella

Received: 9 November 2024
Revised: 24 December 2024
Accepted: 27 December 2024
Published: 17 January 2025

Citation: Panov, D.; Permyakov, G.; Naumov, S.; Mirontsov, V.; Kudryavtsev, E.; Sun, L.; Aksenov, A.; Stepanov, N.; Trushnikov, D.; Salishchev, G. The Effect of Post-Deposition Heat Treatment on the Microstructure, Texture, and Mechanical Properties of Inconel 718 Produced by Hybrid Wire-Arc Additive Manufacturing with Inter-Pass Forging. *Metals* **2025**, *15*, 78. https://doi.org/10.3390/met15010078

1. Introduction

Ni-based superalloys are widely used in the aerospace, petroleum, and chemical industries [1–4] because of their excellent corrosion resistance and good mechanical properties at room temperature and elevated temperatures [5–7]. Meanwhile, most Ni-based superalloys are difficult-to-machine materials with poor weldability and formability [8,9], which are associated with significant issues during the fabrication of parts and structures using conventional techniques. On the other hand, Ni-based superalloys with high Cr,

Fe, and Nb content, of which Inconel 718 is one, have received much attention and wide application due to their good machinability and weldability [10]. Even in Inconel 718, dendritic liquation, porosity in a fusion zone (FZ), and the cracking of a heat-affected zone (HAZ) can happen after welding, which seriously deteriorates the mechanical properties of the obtained welded joints [11,12]. To improve the mechanical properties and prevent cracking of the welded joints, high-frequency microvibrations or ultrasonic treatments are widely applied during welding [13,14]. However, these significantly complicate the manufacturing process.

In recent years, additive manufacturing (AM) has gained wide recognition as a game-changing technology that allows for the efficient fabrication of complex-shaped parts [15–17]. Different AM technologies for producing the parts and structures of Inconel 718 can be used, which are as follows: selective laser melting [18–20], laser/electron beam powder bed fusion [21], electron beam wire-feeding deposition [22], direct metal laser sintering [23], and wire-arc additive manufacturing (WAAM) [24]. It is worth noting that a heterogeneous microstructure, high porosity, residual stress, and hot cracking are often associated with AM technologies [25]. Moreover, the epitaxial growing of columnar grains along the <100> direction over the entire height of the as-printed material [26,27] may result in a strong anisotropy of mechanical properties, as well as reductions in strength and fatigue resistance [28,29].

Among the various AM technologies, WAAM yields high productivity and cost-efficiency [26,30–35]. The careful optimization of WAAM parameters is required to obtain the desired structures and properties [26,36]. For instance, a deposition strategy with an angle of 45° to the overlay direction provides a more homogeneous structure, finer grains, and better mechanical properties in comparison to an angle of 90° [37]. Additionally, to attain an optimal microstructure and optimal mechanical properties, post-deposition heat treatment (PDHT) is essential. The standard heat treatment for wrought products, as per AMS 5662 [38], which can also be used for Inconel 718 after AM [31–33], is solution treatment at 970–980 °C, with soaking for 1 h and further water-quenching, then ageing at 718 °C and soaking for 8 h, with furnace-cooling to 620 °C and soaking at this temperature for 8 h, followed by air-cooling. The solution treatment is associated with the dissolution of the brittle Laves phase, yet needle-shaped δ-phase precipitates on the grain boundaries still remain. These precipitates can provoke intergranular cracking, and hence a lack of ductility [39]. Subsequent ageing can result in strengthening via the precipitation of γ'' phase nanoparticles in the γ-Ni matrix.

The microstructures of as-printed alloys are significantly different from those of wrought products; thus, the standard heat treatment may not be optimal [40]. In the case of Inconel 718 obtained via WAAM, Seow et al. [30] suggest using modified PDHT with the following mode: homogenization at 1186 °C with soaking for 40 min and further air-cooling, then ageing at 720 °C for 8 h with further furnace-cooling to 620 °C, and soaking at this temperature for 8 h, followed by air-cooling. These PDHT results significantly improve mechanical properties via the complete dissolution of the brittle Laves phase and suppression of the needle-shaped δ-phase precipitation. Yet, worse mechanical properties were attained due to the coarse-grained microstructure [30].

In contrast, Xu et al. [33] proposed a new hybrid WAAM and inter-pass cold rolling processing applied to produce Inconel 718 parts with an improved strength–ductility combination. Inter-pass cold rolling prevents the growth of columnar dendrites throughout the as-printed workpiece [32,41]. Grain refining, a reduction in the interdendritic liquation, and texture weakening are obtained [32,42,43]. The parameters of inter-pass cold deformation (temperature, speed, and accumulated plastic strain) affect the microstructure, and, therefore, the mechanical properties of nickel-based superalloys [44,45]. For

instance, due to an increase in plastic strain accumulation during inter-pass cold rolling, the strength and hardness increase due to work hardening, while the ductility decreases [46]. Yet, standard PDHT is conducted after processing, and, therefore, needle-shaped δ-phase precipitates remain.

Apparently, the influence of modified PDHT on the microstructure, texture, and mechanical properties of Inconel 718 billets obtained via WAAM deposition with inter-pass cold deformation has not been investigated. Thus, the present paper will study the effects of modified PDHT on the structure and properties of Inconel 718 obtained through hybrid WAAM–inter-pass cold deformation processing.

2. Materials and Methods

To produce the as-printed material (Inconel 718), the welding wire 3D print AM 718 (BÖHLER, Düsseldorf, Germany) was used. The chemical composition of the welding wire is presented in Table 1. According to an optical emission analysis performed using Foundry Master OE750 (Hitachi, Uedem, Germany), the chemical composition of the as-printed material conformed to the initial wire and standard Inconel 718.

Table 1. Chemical composition of Inconel 718, wt. %.

Condition	Ni	Cr	Fe	Nb	Mo	Ti	Al	C	Si	Mn	Cu	P	B	S
Welding wire	52.29	19.19	18.65	5.25	2.96	0.93	0.48	0.06	0.05	0.02	0.02	0.0032	0.002	0.0014
As-printed	51.98	19.14	18.96	5.28	2.98	0.93	0.47	0.06	0.05	0.02	0.01	0.0029	0.002	0.0008
ASTM B637	50.0–55.0	17.0–21.0	balance	4.75–5.50	2.80–3.30	0.65–1.15	0.20–0.80	<0.08	<0.35	<0.35	<0.30	<0.015	<0.006	<0.015

A wall sample with dimensions of 200 × 90 × 18 mm^3 was produced using a hybrid Cold Metal Transfer (CMT) WAAM and forging setup (Figure 1a,b). The setup was equipped with Fronius welding (welding source, remote control setup, cooling setup, wire feeder, wire buffer, and welding torch (Fronius, Salzburg, Austria)), and forging systems (Airpro, Taichung, Taiwan). The Fronius Trans Puls Synergic 5000 welding source (Fronius, Salzburg, Austria) included an integrated feature set with digital control of CMT processing [47]. The following process parameters were used: an arc current (I) of 140–170 A; an arc voltage (U) of 13–15 V; a wire feed speed (V_{wf}) of 6.0–7.0 m/min; a torch movement speed (V) of 40–50 cm/min; and a shielding gas (argon, ALTERTEKH, Perm, Russia) flow rate (Q) of 25 L/min. The strategy for layer deposition with a 45°/−45° oscillation is shown in Figure 2. At a temperature of 200–300 °C, inter-pass forging over the entire layer was carried out in three passes using a pneumatic hammer (Figure 1c). The temperature range of inter-pass forging was estimated using a pyrometer (SensorTherm, Steinbach, Germany). Temperature control was conducted at the beginning and end of inter-pass forging. The following process parameters were used: a hammer movement speed (V) of 300 mm/min; a hammer blow frequency (N) of 2820 blows/min; an impact energy (E) of 19.74 J; and a pneumatic hammer pressing force of 300 N. The hammer had a semi-spherical shape with a radius (R) of 30 mm. Inter-pass hot forging [48] can disrupt the wall geometry of the as-printed Inconel 718; thus, inter-pass cold forging was conducted at lower temperatures, as shown in Figure 1c. The first two passes forged the edges (A and B). The last pass of inter-pass cold forging deformed the central part of the as-deposited layer (C). The regime of inter-pass cold forging was selected based on the configuration of the pneumatic hammer, ensuring the sufficient process productivity and deformation of each layer by 20 ± 5% without deformation-induced cracking.

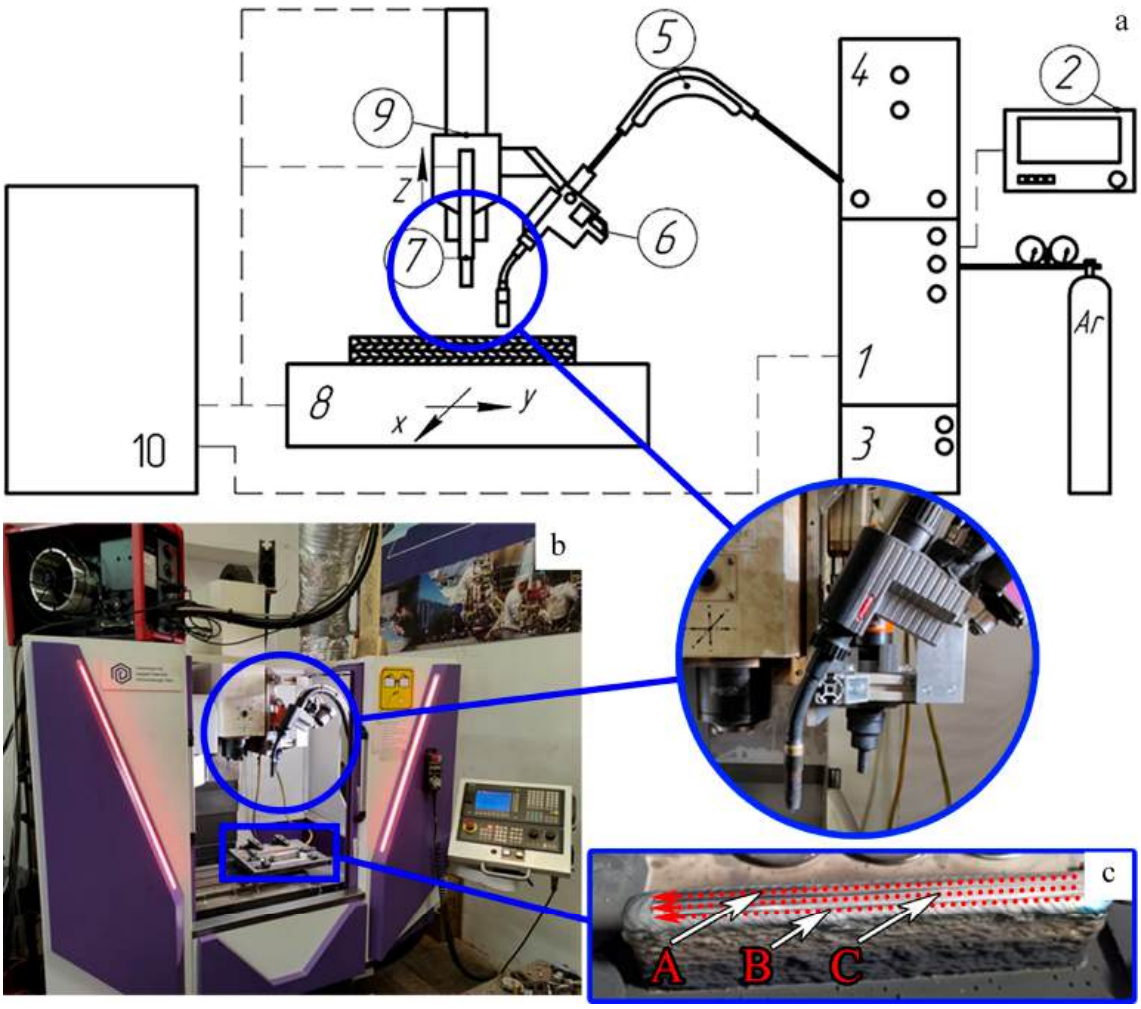

Figure 1. (**a**) A functional scheme of the hybrid CMT-WAAM forging setup (1, current welding source TPS 5000 CMT; 2, remote control setup RCU 5000i; 3, cooling setup FK4000-R; 4, wire-feeding mechanism VR7000-CMT; 5, wire buffer CMT; 6, welding torch Robacta Drive CMT; 7, pneumatic hammer; 8, two-axis table; 9, machining center column; 10, control panel). (**b**) Hybrid Cold Metal Transfer (CMT) WAAM and forging setup and (**c**) as-printed Inconel 718 with inter-pass forging paths (A, 1st pass; B, 2nd pass; C, 3rd pass).

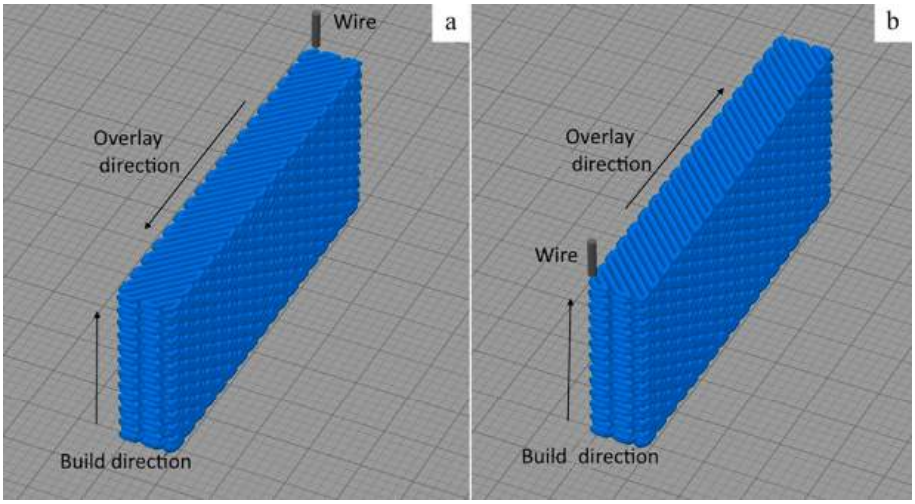

Figure 2. The schemes of the deposition strategy with (**a**) 45° and (**b**) −45° oscillations.

Then, the as-printed sample was subjected to modified PDHT using an EVAK E1300 vacuum furnace (ERSTEVAK, Moscow, Russia) according to the following regime (Figure 3), proposed in Ref. [30]: I, homogenization at 1185 ± 5 °C for 40 min, followed by argon cooling; II, the first ageing step at 720 ± 5 °C for 8 h, followed by furnace-cooling to 620 °C; and III, the second ageing step at 620 ± 5 °C for 8 h and further argon cooling.

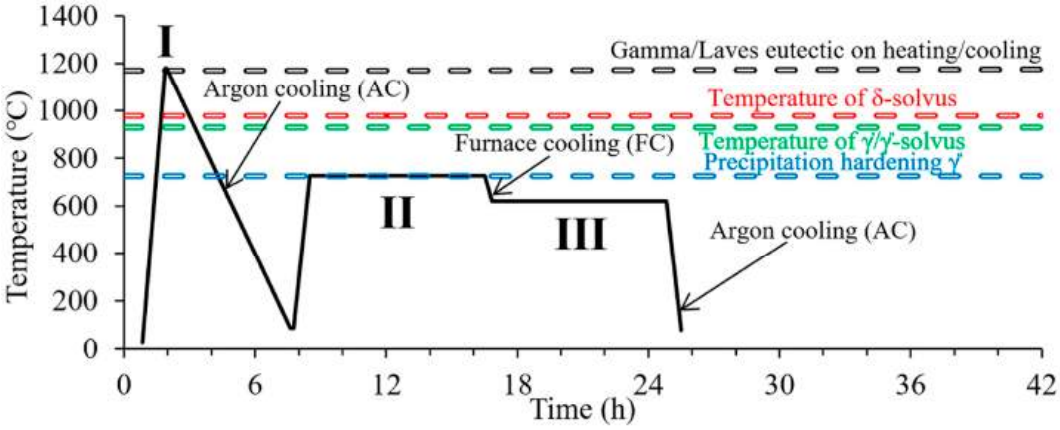

Figure 3. The modified PDHT regime of the as-printed material adapted from [30,49,50].

Samples used for microstructure characterization were grinded, polished (Bainpol VT 10, Chennai Metco, Tamil Nadu, India), and then cleaned using an ultrasonic bath (Sapphire, Moscow, Russia) in pure acetone (Reachem, Moscow, Russia). X-ray diffraction (XRD) analysis was carried out using a SmartLab X-ray diffractometer (Rigaku, Tokyo, Japan) in Cu kα-radiation in an angle range (2θ) of 40–100°, and with a step of 0.05°. The microstructure was characterized in the transverse section using a Nova NanoSEM 450 scanning electron microscope (FEI, Praha, Czech Republic) equipped with a Hikari electron-backscattered diffraction (EBSD) camera, an energy-dispersive spectroscopy (EDS) detector, and a backscattered electron (BSE) detector at an accelerating voltage of 30 kV. Low-resolution EBSD analysis was conducted with a step of 1 μm, while high-resolution EBSD analysis was carried out with a step of 0.2 μm. Two phases (Ni (γ-phase) and Ni_3Ti) were selected during the matching of the Kikuchi patterns. The microstructure and texture parameters were identified using TSL OIM Analysis software (v. 8.5.0). Element distribution maps were obtained at a working distance of 10 mm using APEX software (v. 2.0.0002.0001). The microstructure of the samples was investigated via transmission electron microscopy (TEM), using a JEM-2100 (JEOL, Tokyo, Japan) transmission electron microscope at an accelerating voltage of 200 kV.

Microhardness was measured on the transverse section of the as-printed wall in the build direction. The measurements were carried out with a step of 0.1 mm using a Vickers 402MVD (Instron, Norwood, MA, USA) microhardness tester, with a load of 0.2 kg and a dwell time of 10 s. Microhardness was estimated according to ISO 6507-1 [51]. The measurements were derived for two 10-millimetre-in-length paths per state, and then averaged. Impact toughness and tensile specimens were cut from the as-printed wall sample, as shown in Figure 4a. The dimensions of the specimens are shown in Figures 4b and 4c. The specimens for tensile testing were fabricated based on the standard gauge length of $l_0 = 5.65\sqrt{F_0}$, where F_0 is the transversal section area of the specimen. The specimens were cut in the build direction because this direction is usually considered to be a "weaker" one [31], although inter-pass forging and the applied deposition strategy should provide better profiles of isotropic properties [33,36]. Moreover, the as-printed Inconel 718 did not change significantly by height [52]; therefore, the scheme for cutting samples for mechanical testing used the maximum length of the working part to cover a

larger number of passes. Uniaxial tensile testing was performed at room temperature using an Instron 8802 universal testing machine (Instron, Norwood, MA, USA) with a strain rate of 1×10^{-3} s^{-1}. Impact toughness testing was carried out at room temperature using an Instron 450 MPX pendulum impact testing machine (Instron, Norwood, MA, USA). For each state (as-printed and PDHT), 4 samples were tested.

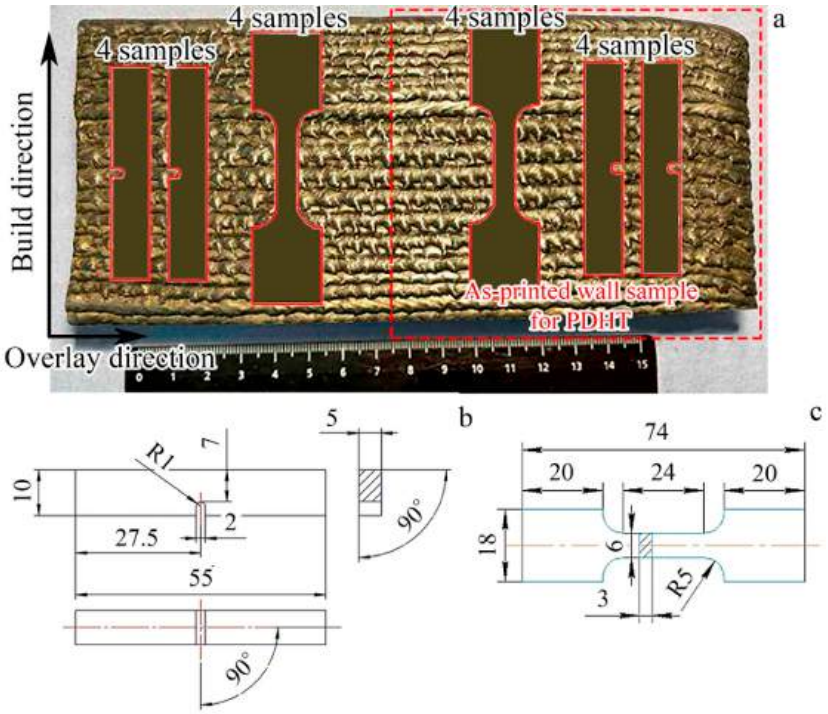

Figure 4. (**a**) A scheme of specimen cutting and sketches of specimens for (**b**) impact toughness (adapted from ISO 148-1 [53]) and (**c**) tensile testing (adapted from ISO 6892 [54]).

3. Results and Discussion

3.1. Microstructure and Texture Characterization

The XRD patterns of the as-printed and PDHT materials are shown in Figure 5. Peaks of the face-centered cubic (FCC) lattice of the γ-Ni matrix were detected. The obtained peaks may have also overlapped with the reflections of the γ′ Ni_3(Al,Ti), γ″ (Ni_3Nb), and δ (Ni_3Nb) phases [55]. After PDHT, the intensities of the (200)γ, (220)γ, and (311)γ peaks decreased significantly, while the intensity of the (111)γ reflection increased. Apparently, this phenomenon may be associated with some changes in the crystallographic texture.

The EBSD analysis of the as-printed and PDHT materials is shown in Figure 6. The as-printed material exhibited two distinct microstructural zones (Figure 6a). The first zone consisted of columnar grains with an average length of 600 ± 250 μm and a thickness of 120 ± 60 μm. The columnar grains had a strong preferred <100> orientation in the build direction, which was associated with the epitaxial growth [26]. The second zone comprised a fully austenitic (according to EBSD) structure with fine-equiaxed grains with an average size of ≈25 ± 15 μm. A random crystallographic orientation in the fine-grained region was observed. According to the kernel average misorientation (KAM) map (Figure 6b), the KAM value gradually increased within the columnar-grained zone from the bottom of the layer to the top. Higher KAM values at the top of these layers are potentially associated with the retained effect of inter-pass forging. However, the opposite tendency was observed in the fine-grained zone, wherein the KAM value decreased from the bottom to the top; i.e., the maximum KAM value was found at the boundary with the previous columnar-grained layer.

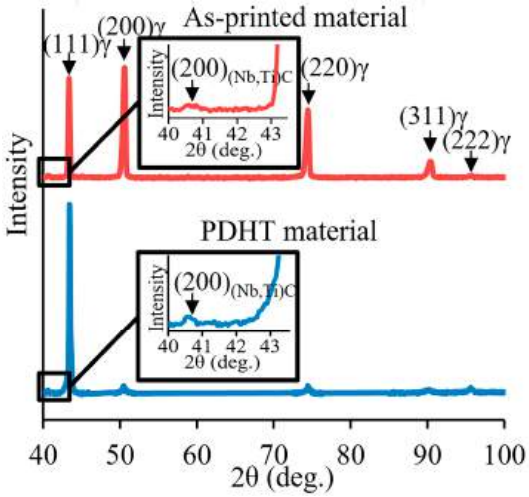

Figure 5. XRD patterns of as-printed and PDHT Inconel 718.

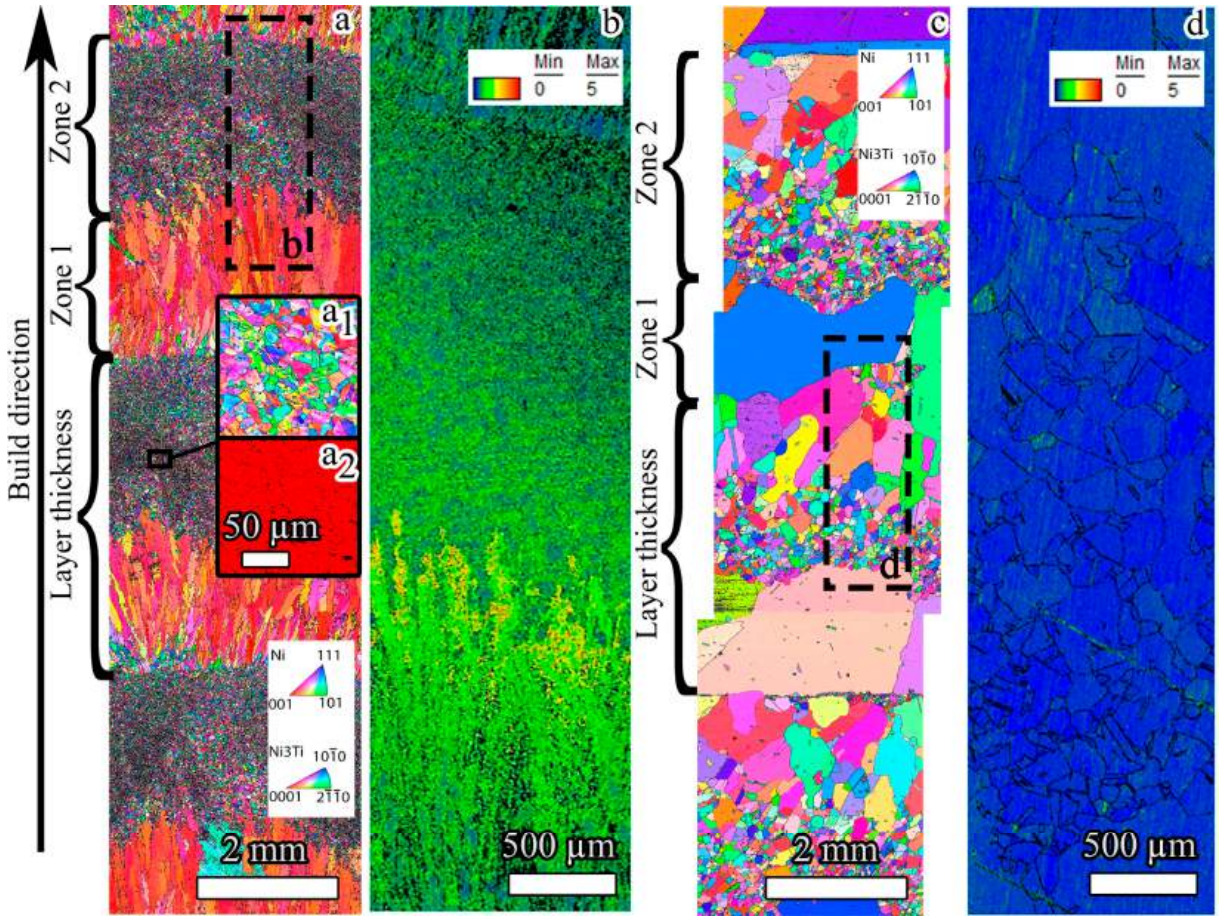

Figure 6. EBSD analysis of (**a**,**b**) as-printed and (**c**,**d**) PDHT Inconel 718 materials: (**a**,**c**) inverse pole figure (IPF) maps and (**b**,**d**) kernel average misorientation (KAM) maps. (**a$_1$**) IPF and (**a$_2$**) phase (red color represents austenite (γ)) maps with higher magnification inserted in (**a**). KAM maps in (**b**,**d**) were collected from cropped areas in (**a**,**c**), respectively.

The microstructure after PDHT was distinctively different from that of the as-printed condition, yet a clear structural inheritance could be found. The following two zones were distinguished (Figure 6c): the first zone was a zone of large uniaxial grains with a diameter of 2.1 ± 0.7 mm; the second zone was a zone with much finer grains and a pronounced grain size gradient ranging from 90 ± 30 μm (upper part) to 0.9 ± 0.2 mm

(lower part). Obviously, the zone of the large grains was formed from the columnar grains via their aggregation growth [30,56] during homogenization at the first stage of PDHT (Figure 3) [57]. Apparently, texture randomization occurred in this zone. In the second zone, gradient strain distribution after inter-pass forging and temperature gradient during the next layer deposition provoked the development of the gradient grain microstructure during homogenization. Obviously, coarser grains were observed in the regions with the higher accumulated strain (i.e., KAM) due to a higher driving force for grain growth [58]. We noted a uniform KAM distribution after PDHT, and low KAM values (Figure 6d). It is worth mentioning that the texture of the as-printed material was not inherited after PDHT. The sharp border between the deposited layers, even after PDHT, was also notable.

SEM-BSE images showed bright particles in the welding wire, as-printed wall, and PDHT material (Figures 7–9). In the welding wire (Figure 7), the particles with irregular and cubic shapes were identified as the Nb-rich Laves phase and (Nb,Ti)C carbides, respectively [59–61]. The volume fraction of both particles was 0.7 ± 0.1% (Figure 10).

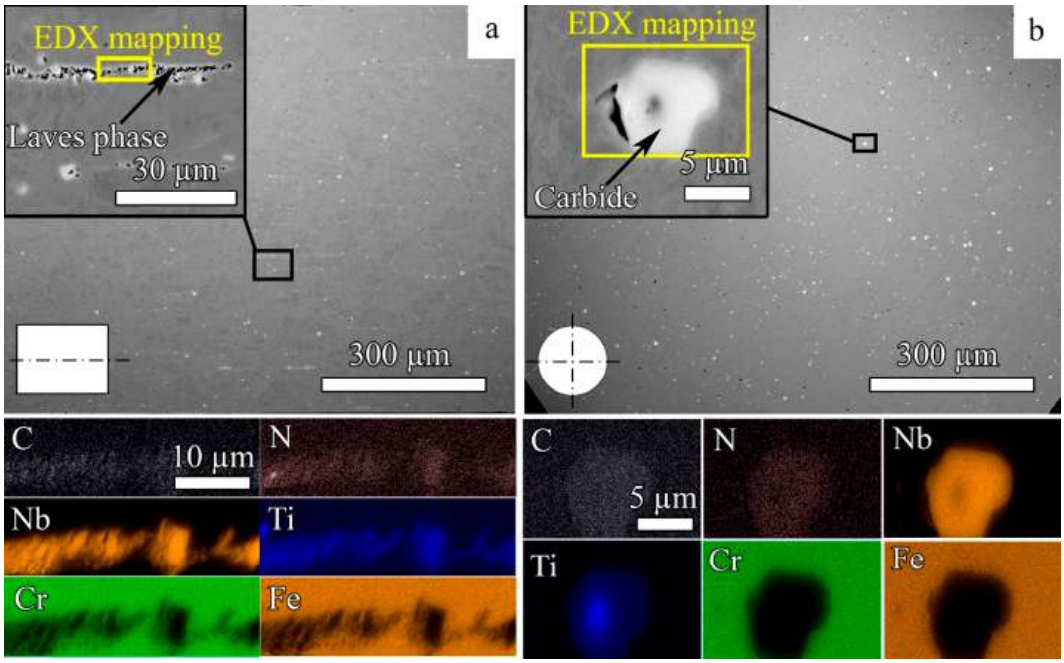

Figure 7. SEM-BSE observations of welding wire 3D print AM 718: (**a**) longitudinal section; (**b**) transverse section. Corresponding results of EDS-analysis are presented in (**a**,**b**).

In the first (columnar-grained) zone of the as-printed material, Laves phase precipitates and (Nb,Ti)C carbides were within the interdendritic space (Figure 8a,b), likely due to dendritic solidification during the WAAM process and elemental segregation herein [32,62,63]. According to Ref. [64], the precipitates were formed via the following mechanism: L → γ → γ + MC carbide → γ + MC carbide + Laves phase. The thickness of the Laves phase precipitates was 2.7 ± 2.2 µm. In the second (fine-grained) zone, Laves phase precipitates were smaller, with an average size of 2.2 ± 1.8 µm (Figure 8c). The refinement of the Laves phase could be attributed to the effect of plastic deformation (the breaking of initial eutectic particles) during inter-pass forging, and their slight dissolution/coagulation could be because of deposition-induced heating. Carbides were also observed herein (Figure 8c), similar to the first zone. However, the volume fraction of the particles was almost the same as that in the welding wire (Figure 10). It is worth mentioning that Ti/N-rich particles (red dashed circle in Figure 8d) may have been the same as TiN nitrides. TiN particles could serve as nucleation sites of NbC carbides during solidification because the two phases were isomorphic [31,65]. According to Ref. [30], the particles were partially inherited

from the welding wire material because their dissolution temperature was higher than the temperature of WAAM processing. It should be noted that the interdendritic micropores in the microstructure of the as-printed material were formed during crystallization (Figure 8a) [26]. Yet, the porosity was very low (the volume fraction was < 0.5%) when using the CMT technique for layer deposition [47] and inter-pass forging [32,33,39]. Obviously, the Laves phase and (Nb,Ti)C carbides were stress concentrators due to their irregular shape and brittleness. Yet, the ductile γ-Ni matrix prevented cracking of the as-printed material during hybrid WAAM processing.

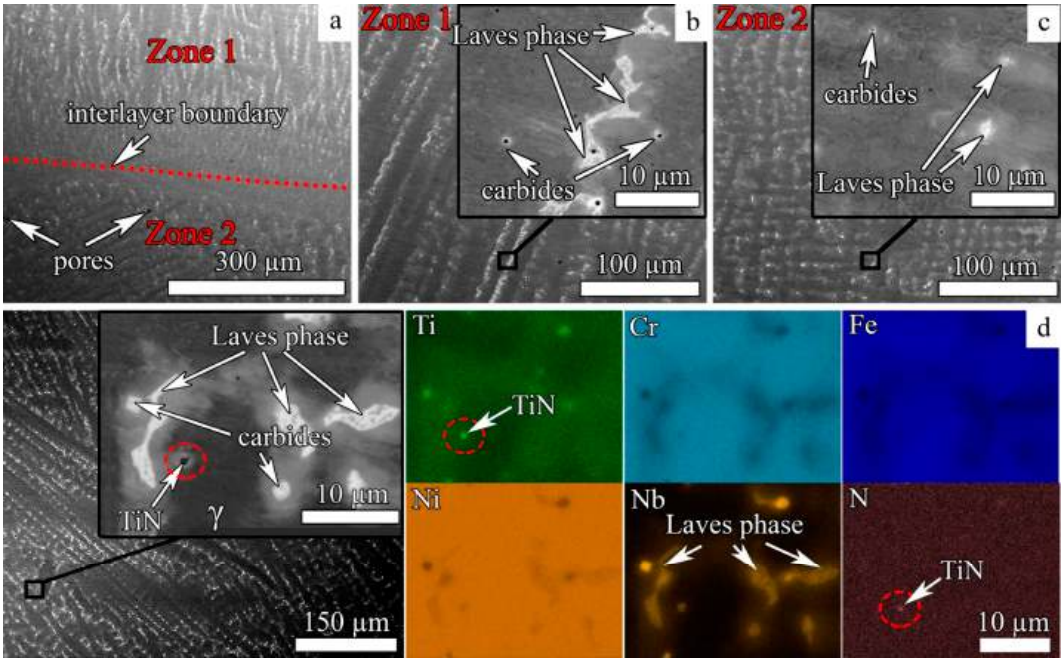

Figure 8. SEM-BSE observations of as-printed Inconel 718: (**a**) interlayer boundary, (**b**) zone 1, (**c**) zone 2, and (**d**) element distribution maps generated via EDS-analysis from the selected region in zone 1.

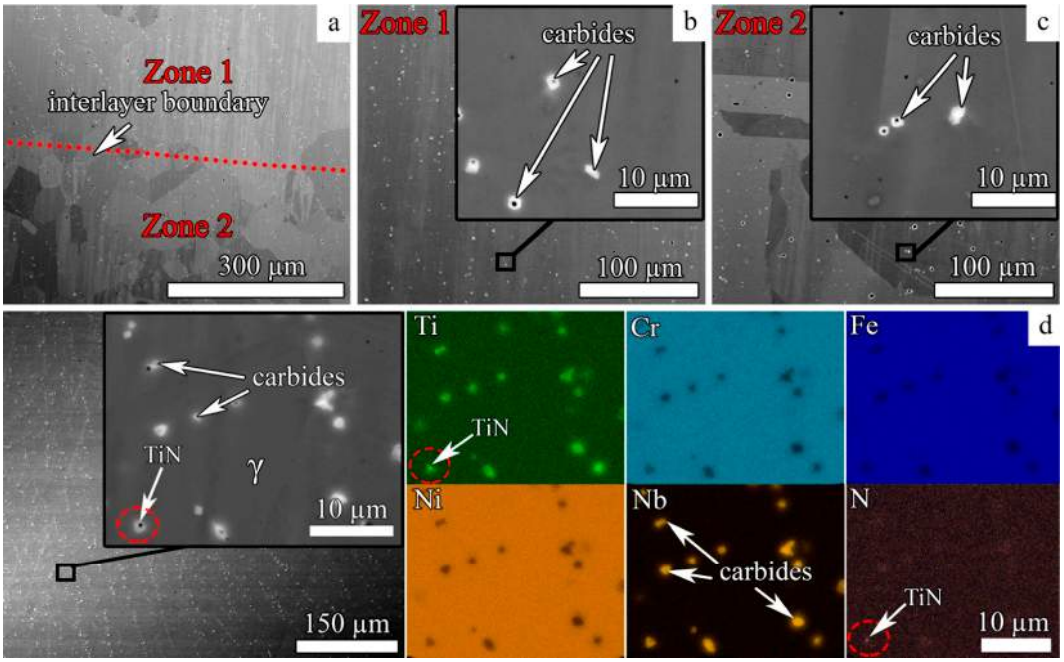

Figure 9. SEM-BSE observations of PDHT Inconel 718: (**a**) interlayer boundary, (**b**) zone 1, (**c**) zone 2, and (**d**) element distribution maps generated via EDS-analysis from the selected region in zone 1.

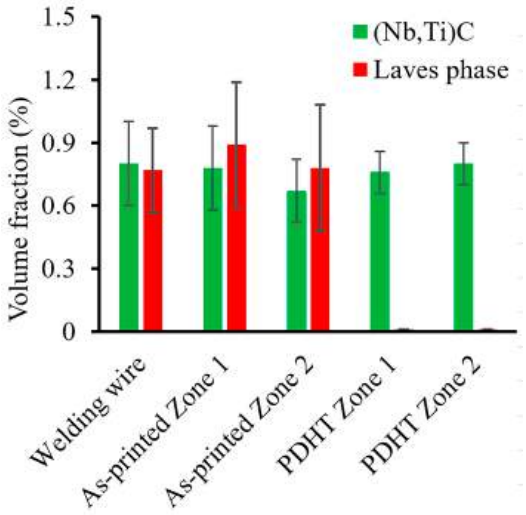

Figure 10. The volume fractions of the Laves phase and (Nb,Ti)C carbides in the welding wire, as-printed wall, and PDHT Inconel 718.

The homogenization of the as-printed material at 1185 °C caused the dissolution of the Laves phase (Figure 9a–c) because the homogenization temperature was higher than the eutectic reaction temperature (Figure 3) [66]. Therefore, the Laves phase was mostly absent in the PDHT material (Figure 10). Only carbides/nitrides of 2.1 ± 0.6 μm in size were preserved (Figure 9d). Indeed, the volume fraction of (Nb,Ti)C carbides was independent of PDHT (Figure 10) because the applied temperatures were lower than the (Nb,Ti)C dissolution temperature [30]. Meanwhile, the γ″ phase precipitated from the γ-Ni matrix during subsequent ageing (Figure 11). The γ″ nanoprecipitates could be observed using selected area electron diffraction and dark-field images (Figure 11b,c). The precipitates had a sandwich-like structure due to the specific ordering reaction [49,67]. The disk-shaped γ″ nanoprecipitates had dimensions of 16 ± 4 nm (diameter) × 5 ± 1 nm (height) (Figure 11b).

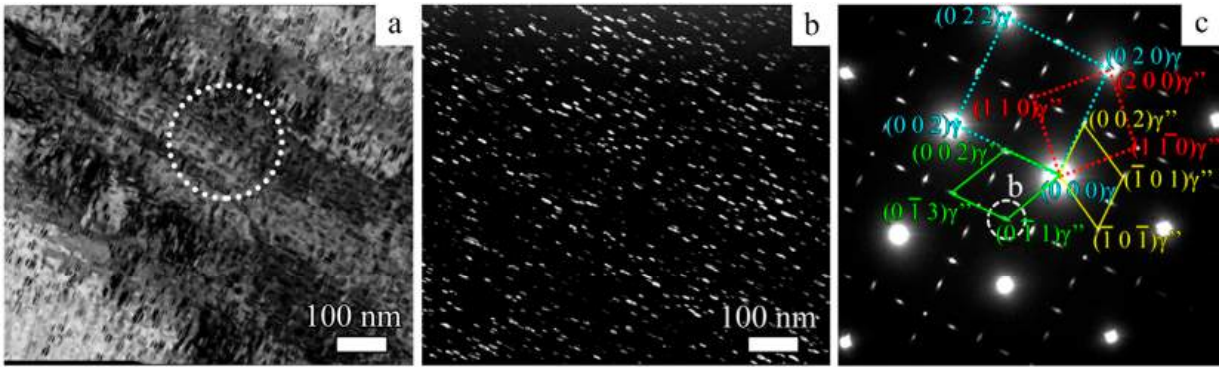

Figure 11. TEM observations of PDHT Inconel 718: (**a**) bright-field image; (**b**) dark-field image in the $(0\bar{1}1)\gamma''$ reflection; (**c**) selected area electron diffraction (SAED) patterns of the ⟨001⟩ γ-Ni zone axis from the field indicated by the dotted circle in (**a**).

3.2. Microhardness and Mechanical Properties

A non-uniform microhardness distribution was observed in the build direction of the as-printed wall (Figure 12a). The fine-grained zone had slightly higher microhardness (318 ± 39 $HV_{0.2}$) compared to the columnar grains (282 ± 23 $HV_{0.2}$), which is in good agreement with earlier papers [19,68]. Inter-pass forging significantly refined the grains, increasing the microhardness value of the as-printed material. PDHT drastically increased the microhardness by 170 $HV_{0.2}$ and resulted in a greater homogeneous microhardness distribution. However, the coarse-grained zone still had the lowest hardness value.

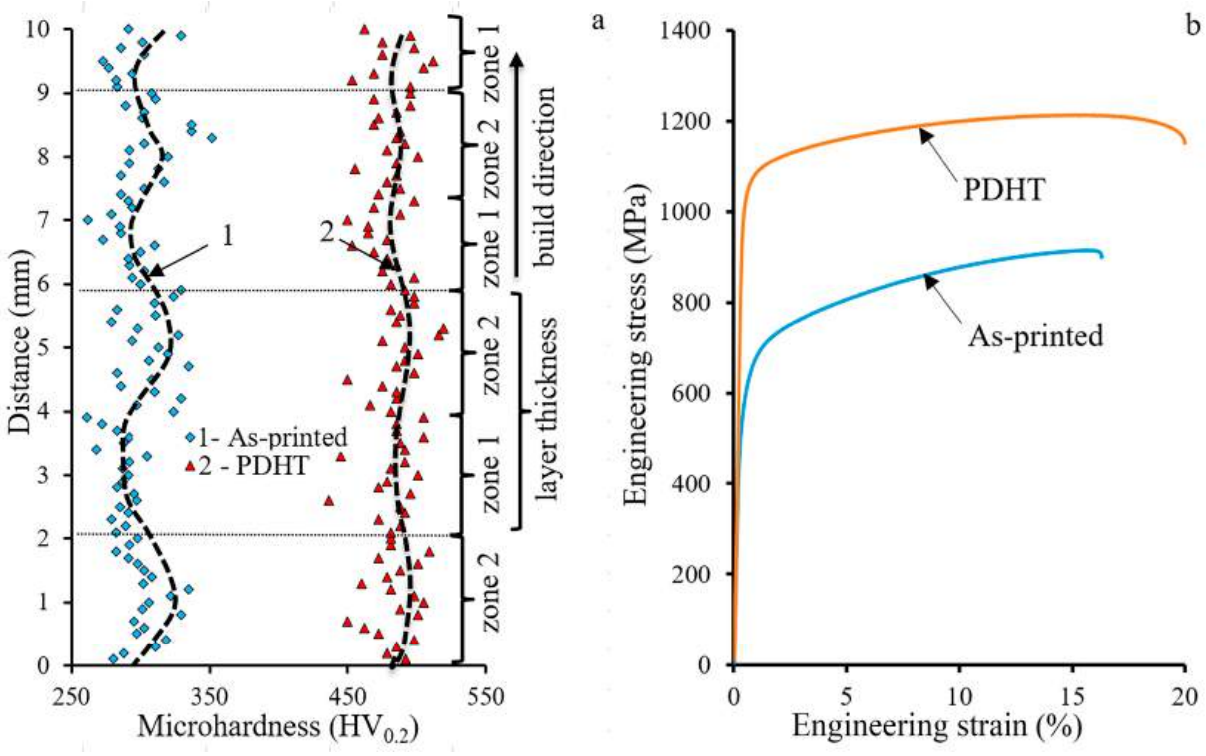

Figure 12. (**a**) Microhardness distribution and (**b**) engineering stress–strain curves of as-printed and PDHT Inconel 718.

The engineering stress–strain curves and the resulting mechanical properties of the as-printed and PDHT Inconel 718 are shown in Figure 12b and Table 2, respectively. The as-printed material possessed modest strength (yield strength (YS) = 530 MPa; ultimate tensile strength (UTS) = 800 MPa). After PDHT, significant strengthening (YS = 1020 MPa; UTS = 1160 MPa) occurred. Surprisingly, PDHT somewhat increased ductility (ultimate elongation (UE) increased from 14–17%; reduction in area (RA) increased from 18–23%). It should be noted that the welding wire had high strength and ductility simultaneously (Table 2). Although, in both Inconel 718 conditions, specimens demonstrated mostly ductile fractures (Figure 13), many secondary microcracks were detected near and within the Laves phase-containing eutectic regions in the as-printed material (Figure 14a). Meanwhile, in the PDHT material, a few microcracks were found inside and along the carbides (Figure 14b). The impact toughness of the as-printed material (Table 2) was quite high (65 J/cm^2). After PDHT, the impact toughness increased to 80 J/cm^2. The fracture of the as-printed material was macroscopically flat, but microgrooves were detected (Figure 15a–c). PDHT caused a uniform, ductile-dimpled fracture (Figure 15d–f).

Table 2. Mechanical properties of Inconel 718.

Condition	UTS, MPa	YS, MPa	UE, %	RA, %	KCU, J/cm^2
As-printed	800 ± 98	530 ± 34	14 ± 10	18 ± 9	65 ± 10
PDHT	1160 ± 85	1020 ± 17	17 ± 10	23 ± 11	80 ± 4
Welding wire 3D-printed AM 718	1150 ± 15	805 ± 10	25 ± 5	36 ± 13	-

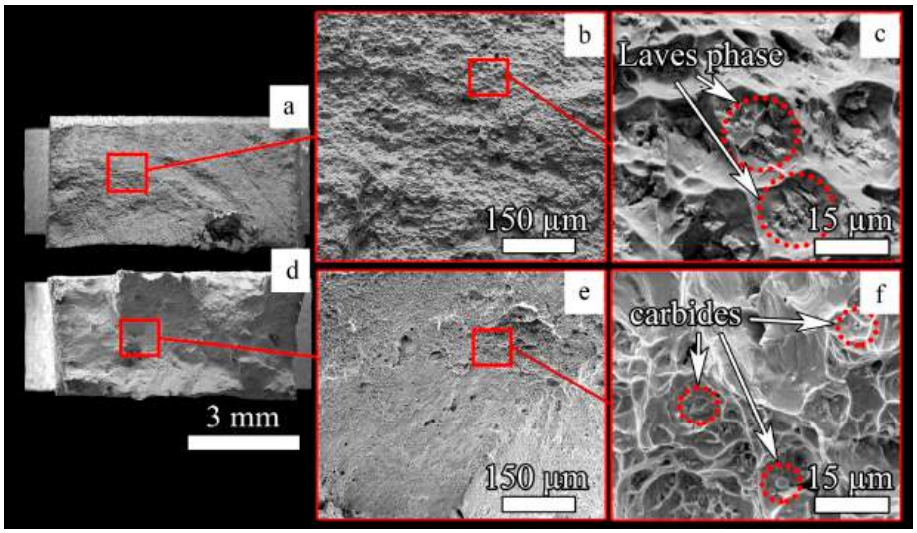

Figure 13. Fracture overview and microphotographs of tensile specimens of (**a**–**c**) as-printed and (**d**–**f**) PDHT Inconel 718.

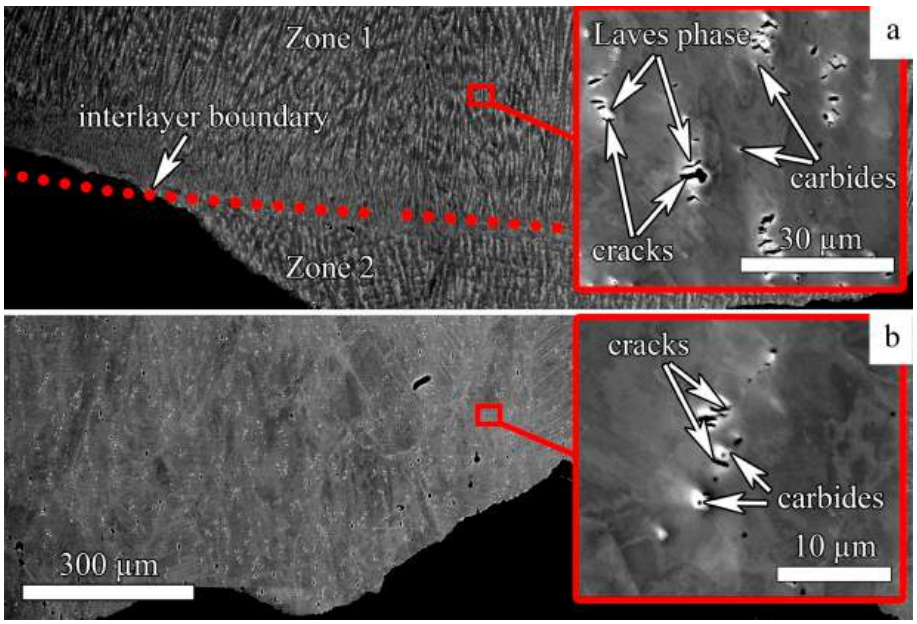

Figure 14. Fracture profiles of tensile specimens of (**a**) as-printed and (**b**) PDHT Inconel 718.

Hybrid WAAM with inter-pass forging produced the as-printed wall with the layered bimodal microstructure, consisting of columnar- and fine-grained zones (Figure 6a). The fine-grained zone formation was ascribed to non-uniform plastic strain distribution after inter-pass forging and the subsequent static recrystallization of the deformed material during the deposition of the next (upper) layer [33]. Indeed, non-uniform temperature distribution and, therefore, more-developed recrystallization in the upper part of the previous layer during processing, defined the gradient distribution of the KAM value in the build direction (Figure 6b). The development of columnar grains throughout interlayer boundaries was suppressed, which, according to Refs. [28,29], promoted the reduced anisotropy of mechanical properties, higher strength, and fatigue resistance. However, (Nb,Ti)C carbides, TiN nitrides, and Laves phase precipitates promoted premature failure during the mechanical testing of the as-printed material [69]. The precipitates served as stress concentrators [70] and, thus, provoked early microcrack nucleation (Figure 14a). Furthermore, microgrooves on the fracture surface after impact testing (Figure 15a–c) and

the decreased impact toughness value (Table 2) were related to simplified crack growth along the rows of the brittle precipitates (Figure 8). On the other hand, the layered bimodal microstructure (Figure 6a) was associated with the enhanced impact toughness value of the as-printed material if crack propagation occurred throughout different zones [71].

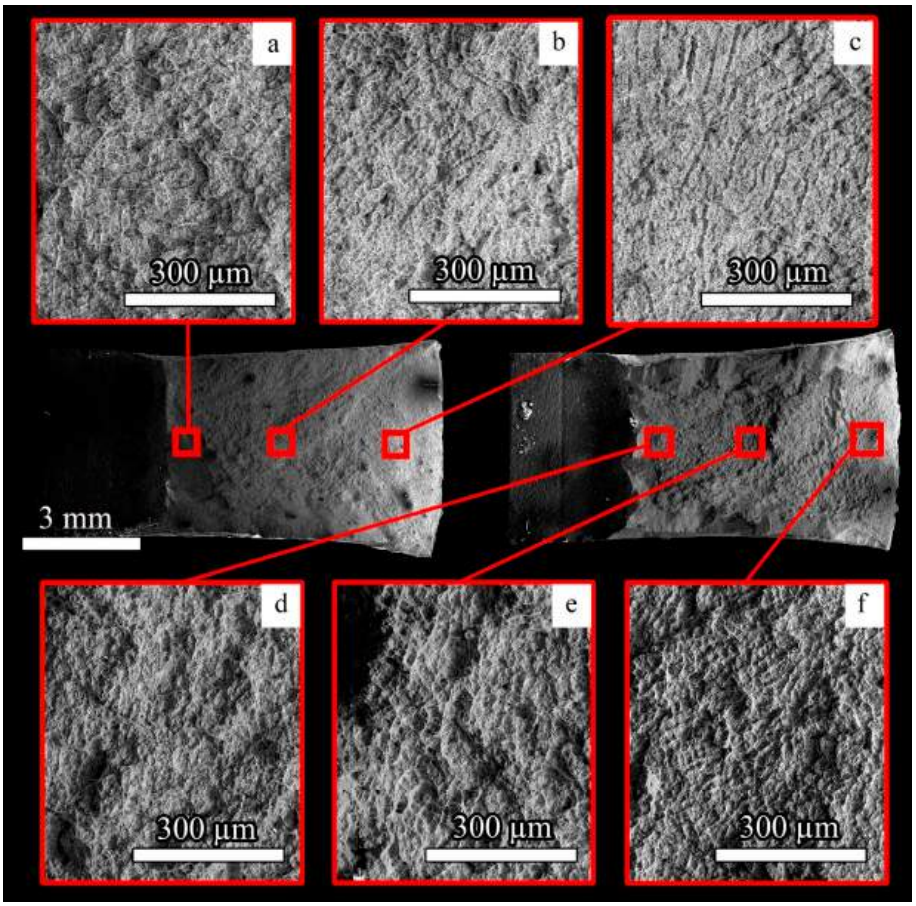

Figure 15. Fracture overview and microphotographs of impact toughness specimens of (**a**–**c**) as-printed and (**d**–**f**) PDHT Inconel 718.

Subsequent PDHT resulted in significant hardening and strengthening, as well as increases in ductility and impact toughness (Table 2). Apparently, the observed phase evolution strongly affected the mechanical properties of the program material. The improvements in ductility and impact toughness (Table 2) could be attributed to the dissolution of the brittle Laves phase at the first step (homogenization) of PDHT (Figures 9 and 10), causing minor microcracking under tension (Figure 14b) and ductile-dimpled fracture during impact testing (Figure 15d–f). At the second and third steps (ageing), increases in hardness and strength were caused by precipitation of γ'' nanoparticles in the γ-Ni matrix (Figure 11) due to the dispersion-strengthening effect [19,72]. Contrarily, significant grain coarsening after PDHT (Figure 6) supposedly caused softening due to the Hall–Petch effect [73,74]. Yet, a negligible effect of grain size on ductility was anticipated [75]. Interestingly, the obtained microstructure of the PDHT material could transform during and following use. According to Ref. [76], long-term (3000 h) thermal cycling of Inconel 718 induced a phase transformation of the metastable γ'' into a stable intragranular δ-phase. Therefore, a several-percent decrease in mechanical properties was determined after the thermal cycling.

In comparison to the data of other works that considered CMT/Plasma-WAAM processing, the proposed strength–ductility combination was equal to the best results produced via hybrid WAAM–rolling processing with the standard/modified PDHT

(Figure 16) [30,31,33,39,77,78]. Meanwhile, the wrought Inconel 718 possessed lower ductility (UE = 12%) [79] in comparison to the PDHT Inconel 718 (UE = 17%), while the strength value was nearly the same (YS = 1020–1060 MPa). The improved UE of the PDHT Inconel 718 could be compared to the absence of needle-shaped δ-phase precipitates that formed during the standard heat treatment (as per AMS 5662) of the wrought Inconel 718. In turn, the precipitates promoted intergranular cracking, and, therefore, a lack of ductility [39]. Thus, hybrid CMT-WAAM–forging processing and subsequent modified PDHT is a promising technique that helped us to fabricate large parts and constructions with attractive mechanical properties.

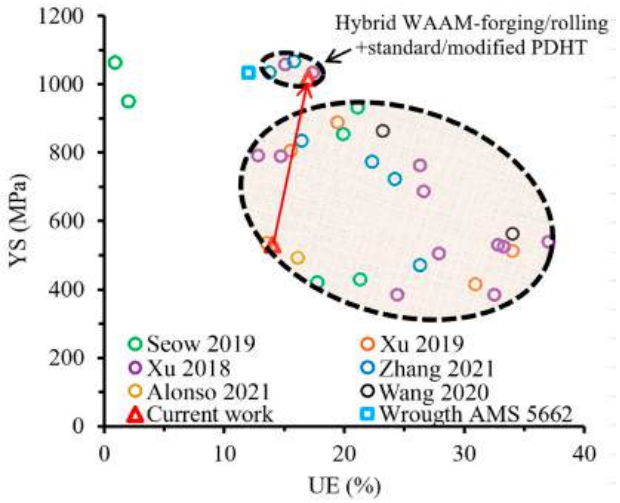

Figure 16. Yield strength (YS) and ultimate elongation (UE) combination of Inconel 718 obtained using CMT/Plasma-WAAM processing adapted from [30,31,33,39,77,78].

The proposed approach has enabled researchers to produce large parts with exceptional quality and high repeatability, using simple equipment on a single platform (CMT welding torch and hammer) for the oil and gas industry, as well as the nuclear industry [80–82]. It is also worth noting that CMT-WAAM processing was highly efficient, whereas inter-pass forging resulted in good mechanical properties for the as-printed material (Inconel 718).

One future direction of our research is the study of the effects of the hybrid WAAM–inter-pass forging approach on the microstructures and mechanical properties of as-printed walls produced from other structural materials (Inconel 625, maraging steels, and others) and the development of post-deposition heat treatment regimes.

4. Conclusions

The effect that modified post-deposition heat treatment (Step I, homogenization at 1185 ± 5 °C for 40 min with argon cooling; Step II, the first ageing step at 720 ± 5 °C for 8 h, followed by furnace-cooling to 620 °C; Step III, the second ageing step at 620 ± 5 °C for 8 h with argon cooling) had on the microstructure, texture, and mechanical properties of Inconel 718 fabricated via hybrid wire-arc additive manufacturing with inter-pass forging was studied. The following conclusions were drawn:

1. The as-printed material possessed a layered bimodal microstructure, consisting of a columnar-grained zone with a <100> orientation, and a fine-grained zone with a random crystallographic orientation. The fine-grained zone was formed via static recrystallization induced through inter-pass forging and further heating during the deposition of the next (upper) layer. Particles of (Nb,Ti)C and TiN and precipitates

of the Nb-rich Laves phase were found in the as-printed alloy. The Laves phase precipitates provoked premature cracking and failure during mechanical testing.

2. After modified post-deposition heat treatment, the following two zones were observed: (i) a coarse-grained zone and (ii) a gradient-grained zone. Texture randomization also occurred. The dissolution of the brittle Laves phase and precipitation of γ'' nanoparticles were observed during homogenization and ageing, respectively.
3. Modified post-deposition heat treatment of the hybrid wire-arc additively manufactured components with inter-pass forging resulted in simultaneous increases in strength, ductility, and impact toughness. For instance, the yield strength increased from 530–1020 MPa, elongation to fracture increased from 18–23%, and impact toughness increased from 65–80 J/cm^2.

Author Contributions: Conceptualization, D.T. and G.S.; methodology, D.P., G.P., S.N., V.M., E.K. and A.A.; formal analysis and investigation, D.P., G.P., S.N., V.M., E.K. and A.A.; writing—original draft preparation, D.P., G.P. and S.N.; visualization, N.S. and L.S.; writing—review and editing, N.S., G.S., and L.S.; funding acquisition, N.S. and D.T.; resources, D.T. and G.S.; supervision, D.T. and G.S. All authors have read and agreed to the published version of the manuscript.

Funding: A part of this research (electron microscopic research, microhardness characterization, and X-ray diffraction analysis) was partially funded by the Russian Science Foundation (grant No. 23-19-00622; https://rscf.ru/en/project/23-19-00622/, accessed on 27 December 2023). The fabrication of the material and mechanical tests was carried out with the financial support of the Ministry of Science and Higher Education of the Russian Federation as part of the national project "Science and Universities" and the state task "development of scientific and technological foundations for the formation of a material-structure system with special properties based on hybrid additive technologies"—FSNM-2024-0003.

Data Availability Statement: The original contributions presented in this study are included in the article. Further inquiries can be directed to the corresponding authors.

Acknowledgments: The authors would like to thank Evlashin S. and Zherebtsov S. for their support during the course of this study. The authors are grateful to the personnel of the Joint Research Center, "Technology and Materials", at the Belgorod National Research University, for their assistance.

Conflicts of Interest: The authors declare no conflicts of interest.

References

1. Ghiban, B.; Elefterie, C.F.; Guragata, C.; Bran, D. Requirements of Inconel 718 alloy for aeronautical applications. *AIP Conf. Proc.* **2018**, *1932*, 30016. [CrossRef]
2. Debarbadillo, J.J.; Mannan, S.K. Alloy 718 for oilfield applications. *Jom* **2012**, *64*, 265–270. [CrossRef]
3. Reed, R.C. *The Superalloys: Fundamentals and Applications*; Cambridge University Press: Cambridge, UK, 2008; ISBN 9780521070119.
4. Pollock, T.M.; Tin, S. Nickel-based superalloys for advanced turbine engines: Chemistry, microstructure, and properties. *J. Propuls. Power* **2006**, *22*, 361–374. [CrossRef]
5. Elefterie, C.F.; Guragata, C.; Bran, D.; Ghiban, B. Aeronautical requirements for Inconel 718 alloy. *IOP Conf. Ser. Mater. Sci. Eng.* **2017**, *209*, 12060. [CrossRef]
6. Kladovasilakis, N.; Tsongas, K.; Tzetzis, D. Finite element analysis of orthopedic hip implant with functionally graded bioinspired lattice structures. *Biomimetics* **2020**, *5*, 44. [CrossRef]
7. Achitei, D.C.; Baltatu, M.S.; Vizureanu, P.; Sandu, A.V.; Benchea, M.; Istrate, B. Ni-Cr Alloys Assessment for Dental Implants Suitability. *Appl. Sci.* **2022**, *12*, 12814. [CrossRef]
8. Arunachalam, R.; Mannan, M.A. Machinability of nickel-based high temperature alloys. *Mach. Sci. Technol. Int. J.* **2000**, *4*, 127–168. [CrossRef]
9. DuPont, J.N.; Lippold, J.C.; Kiser, S.D. *Welding Metallurgy and Weldability of Nickel-Base Alloys*; Wiley: Hoboken, NJ, USA, 2009; ISBN 9780470500262.
10. Tabaie, S.; Rézaï-Aria, F.; Jahazi, M. Microstructure evolution of selective laser melted inconel 718: Influence of high heating rates. *Metals* **2020**, *10*, 587. [CrossRef]

11. Sonar, T.; Balasubramanian, V.; Malarvizhi, S.; Venkateswaran, T.; Sivakumar, D. An overview on welding of Inconel 718 alloy—Effect of welding processes on microstructural evolution and mechanical properties of joints. *Mater. Charact.* **2021**, *174*, 110997. [CrossRef]
12. Cao, X.; Rivaux, B.; Jahazi, M.; Cuddy, J.; Birur, A. Effect of pre- and post-weld heat treatment on metallurgical and tensile properties of Inconel 718 alloy butt joints welded using 4 kW Nd:YAG laser. *J. Mater. Sci.* **2009**, *44*, 4557–4571. [CrossRef]
13. Bai, Y.; Lu, Q.; Ren, X.; Yan, H.; Zhang, P. Study of inconel 718 welded by bead-on-plate laser welding under high-frequency micro-vibration condition. *Metals* **2019**, *9*, 1335. [CrossRef]
14. Thavamani, R.; Balusamy, V.; Nampoothiri, J.; Subramanian, R.; Ravi, K.R. Mitigation of hot cracking in Inconel 718 superalloy by ultrasonic vibration during gas tungsten arc welding. *J. Alloys Compd.* **2018**, *740*, 870–878. [CrossRef]
15. Froes, F.H.; Boyer, R. *Additive Manufacturing for the Aerospace Industry*, 1st ed.; Francis, H., Froes, R.B., Eds.; Elsevier: Amsterdam, The Netherlands, 2019; ISBN 9780128140628.
16. *ISO-ASTM-52900*; Additive Manufacturing—General Principles—Fundamentals and Vocabulary. International Standard: Geneva, Switzerland, 2021; p. 28.
17. Yusuf, S.M.; Cutler, S.; Gao, N. Review: The impact of metal additive manufacturing on the aerospace industry. *Metals* **2019**, *9*, 1286. [CrossRef]
18. Chlebus, E.; Gruber, K.; Kuźnicka, B.; Kurzac, J.; Kurzynowski, T. Effect of heat treatment on the microstructure and mechanical properties of Inconel 718 processed by selective laser melting. *Mater. Sci. Eng. A* **2015**, *639*, 647–655. [CrossRef]
19. Ni, M.; Liu, S.; Chen, C.; Li, R.; Zhang, X.; Zhou, K. Effect of heat treatment on the microstructural evolution of a precipitation-hardened superalloy produced by selective laser melting. *Mater. Sci. Eng. A* **2019**, *748*, 275–285. [CrossRef]
20. Sufiiarov, V.; Erutin, D.; Borisov, E.; Popovich, A. Selective laser melting of Inconel 718/TiC composite: Effect of TiC particle size. *Metals* **2022**, *12*, 1729. [CrossRef]
21. Ghorbanpour, S.; Deshmukh, K.; Sahu, S.; Riemslag, T.; Reinton, E.; Borisov, E.; Popovich, A.; Bertolo, V.; Jiang, Q.; Sanchez, M.T.; et al. Additive manufacturing of functionally graded inconel 718: Effect of heat treatment and building orientation on microstructure and fatigue behaviour. *J. Mater. Process. Technol.* **2022**, *306*, 117573. [CrossRef]
22. Osipovich, K.; Kalashnikov, K.; Chumaevskii, A.; Gurianov, D.; Kalashnikova, T.; Vorontsov, A.; Zykova, A.; Utyaganova, V.; Panfilov, A.; Nikolaeva, A.; et al. Wire-Feed Electron Beam Additive Manufacturing: A Review. *Metals* **2023**, *13*, 279. [CrossRef]
23. Raj, B.A.; Jappes, J.T.W.; Khan, M.A.; Dillibabu, V.; Brintha, N.C. Direct metal laser sintered (DMLS) process to develop Inconel 718 alloy for turbine engine components. *Optik* **2020**, *202*, 163735. [CrossRef]
24. Maronek, M.; Sugra, F.; Bartova, K.; Barta, J.; Dománková, M.; Urminsky, J.; Pasak, M. The Effect of Interpass Temperature on the Mechanical Properties and Microstructure of Components Made by the WAAM Method from Inconel 718 Alloy. *Metals* **2024**, *14*, 953. [CrossRef]
25. Singh, S.; Andersson, J. Hot cracking in cast alloy 718. *Sci. Technol. Weld. Join.* **2018**, *23*, 568–574. [CrossRef]
26. Kindermann, R.M.; Roy, M.J.; Morana, R.; Francis, J.A. Effects of microstructural heterogeneity and structural defects on the mechanical behaviour of wire + arc additively manufactured Inconel 718 components. *Mater. Sci. Eng. A* **2022**, *839*, 142826. [CrossRef]
27. Calandri, M.; Yin, S.; Aldwell, B.; Calignano, F.; Lupoi, R.; Ugues, D. Texture and microstructural features at different length scales in Inconel 718 produced by selective laser melting. *Materials* **2019**, *12*, 1293. [CrossRef] [PubMed]
28. Mostafa, A.; Rubio, I.P.; Brailovski, V.; Jahazi, M.; Medraj, M. Structure, texture and phases in 3D printed IN718 alloy subjected to homogenization and HIP treatments. *Metals* **2017**, *7*, 96. [CrossRef]
29. Zerbst, U.; Bruno, G.; Buffière, J.Y.; Wegener, T.; Niendorf, T.; Wu, T.; Zhang, X.; Kashaev, N.; Meneghetti, G.; Hrabe, N.; et al. Damage tolerant design of additively manufactured metallic components subjected to cyclic loading: State of the art and challenges. *Prog. Mater. Sci.* **2021**, *121*, 100786. [CrossRef]
30. Seow, C.E.; Coules, H.E.; Wu, G.; Khan, R.H.U.; Xu, X.; Williams, S. Wire + Arc Additively Manufactured Inconel 718: Effect of post-deposition heat treatments on microstructure and tensile properties. *Mater. Des.* **2019**, *183*, 108157. [CrossRef]
31. Xu, X.; Ding, J.; Ganguly, S.; Williams, S. Investigation of process factors affecting mechanical properties of INCONEL 718 superalloy in wire + arc additive manufacture process. *J. Mater. Process. Technol.* **2019**, *265*, 201–209. [CrossRef]
32. Hönnige, J.; Seow, C.E.; Ganguly, S.; Xu, X.; Cabeza, S.; Coules, H.; Williams, S. Study of residual stress and microstructural evolution in as-deposited and inter-pass rolled wire plus arc additively manufactured Inconel 718 alloy after ageing treatment. *Mater. Sci. Eng. A* **2021**, *801*, 140368. [CrossRef]
33. Xu, X.; Ganguly, S.; Ding, J.; Seow, C.E.; Williams, S. Enhancing mechanical properties of wire + arc additively manufactured INCONEL 718 superalloy through in-process thermomechanical processing. *Mater. Des.* **2018**, *160*, 1042–1051. [CrossRef]
34. Zou, X.; Niu, B.; Pan, L.; Yi, J. Wire + Arc Additive Manufacturing and Heat Treatment of Super Martensitic Stainless Steel with a Refined Microstructure and Excellent Mechanical Properties. *Materials* **2022**, *15*, 2624. [CrossRef]
35. Karouanas, I.; Foteinopoulos, P.; Bikas, H.; Stavropoulos, P. A practical simulation approach for the support of wire arc DED additive manufacturing systems design. *Procedia Comput. Sci.* **2024**, *232*, 3161–3172. [CrossRef]

36. Xi, N.; Tang, K.; Fang, X.; Li, Y.; Duan, Y.; Huang, K. Enhanced comprehensive properties of directed energy deposited Inconel 718 by a novel integrated deposition strategy. *J. Mater. Sci. Technol.* **2023**, *141*, 42–55. [CrossRef]
37. Su, C.; Chen, X.; Konovalov, S.; Singh, R.A.; Jayalakshmi, S.; Huang, L. Effect of Deposition Strategies on the Microstructure and Tensile Properties of Wire Arc Additive Manufactured Al-5Si Alloys. *J. Mater. Eng. Perform.* **2021**, *30*, 2136–2146. [CrossRef]
38. *AMS 5662*; Alloy Bars, Forgings, and Rings, Corrosion and Heat Resistant. Nickel Base-19Cr-3.1Mo-5.1(Cb + Ta)-0.90Ti-0.50Al Consumable Electrode or Vacuum Induction Melted, Solution Treated. SAE In-ternational: Warrendale, PA, USA, 1965. [CrossRef]
39. Zhang, T.; Li, H.; Gong, H.; Wu, Y.; Ahmad, A.S.; Chen, X. Effect of rolling force on tensile properties of additively manufactured Inconel 718 at ambient and elevated temperatures. *J. Alloys Compd.* **2021**, *884*, 161050. [CrossRef]
40. Laleh, M.; Sadeghi, E.; Revilla, R.I.; Chao, Q.; Haghdadi, N.; Hughes, A.E.; Xu, W.; De Graeve, I.; Qian, M.; Gibson, I.; et al. Heat treatment for metal additive manufacturing. *Prog. Mater. Sci.* **2023**, *133*, 101051. [CrossRef]
41. Farias, F.W.C.; dos Santos, T.J.G.; Oliveira, J.P. Directed energy deposition + mechanical interlayer deformation additive manufacturing: A state-of-the-art literature review. *Int. J. Adv. Manuf. Technol.* **2024**, *131*, 999–1038. [CrossRef]
42. Dong, R.; Li, J.; Chen, Z.; Zhang, W.; Zhou, X. Effect of Deformation Degree on Microstructure and Properties of Ni-Based Alloy Forgings. *Metals* **2024**, *14*, 340. [CrossRef]
43. Chamanfar, A.; Sarrat, L.; Jahazi, M.; Asadi, M.; Weck, A.; Koul, A.K. Microstructural characteristics of forged and heat treated Inconel-718 disks. *Mater. Des.* **2013**, *52*, 791–800. [CrossRef]
44. Guimaraes, A.A.; Jonas, J.J. Recrystallization and aging effects associated with the high temperature deformation of waspaloy and inconel 718. *Metall. Trans. A* **1981**, *12*, 1655–1666. [CrossRef]
45. Nowotnik, A. Mechanical and structural aspects of high temperature deformation in Ni alloy. *J. Achiev. Mater. Manuf. Eng.* **2008**, *26*, 115–122.
46. Tucho, W.M.; Sletsjøe, A.T.; Sayyar, N.; Hansen, V. Optimizing Tensile Properties and Hardness of Inconel 718 by Cold Rolling. *Metals* **2024**, *14*, 455. [CrossRef]
47. Selvi, S.; Vishvaksenan, A.; Rajasekar, E. Cold metal transfer (CMT) technology—An overview. *Def. Technol.* **2018**, *14*, 28–44. [CrossRef]
48. Duarte, V.R.; Rodrigues, T.A.; Schell, N.; Miranda, R.M.; Oliveira, J.P.; Santos, T.G. Hot forging wire and arc additive manufacturing (HF-WAAM). *Addit. Manuf.* **2020**, *35*, 101193. [CrossRef]
49. Sadek, A. Optimization of the Post Heat Treatment of Additively Manufactured IN718. *J. Mater. Eng. Perform.* **2024**, *33*, 4265–4277. [CrossRef]
50. Antonsson, T.; Fredriksson, H. The effect of cooling rate on the solidification of INCONEL 718. *Metall. Mater. Trans. B* **2005**, *36*, 85–96. [CrossRef]
51. *ISO 6507-1*; Metallic Materials—Vickers Hardness Test—Part 1: Test Method. ISO: Geneva, Switzerland, 2023.
52. Wang, X.; Keya, T.; Chou, K. Build Height Effect on the Inconel 718 Parts Fabricated by Selective Laser Melting. *Procedia Manuf.* **2016**, *5*, 1006–1017. [CrossRef]
53. *ISO 148-1*; Metallic Materials—Charpy Pendulum Impact Test—Part 1: Test Method. ISO: Geneva, Switzerland, 2016.
54. *ISO 6892-1*; Metallic Materials—Tensile Testing—Part 1: Method of Test at Room Temperature. ISO: Geneva, Switzerland, 2009.
55. Dinda, G.P.; Dasgupta, A.K.; Mazumder, J. Laser aided direct metal deposition of Inconel 625 superalloy: Microstructural evolution and thermal stability. *Mater. Sci. Eng. A* **2009**, *509*, 98–104. [CrossRef]
56. Seede, R.; Mostafa, A.; Brailovski, V.; Jahazi, M.; Medraj, M. Microstructural and microhardness evolution from homogenization and hot isostatic pressing on selective laser melted inconel 718: Structure, texture, and phases. *J. Manuf. Mater. Process.* **2018**, *2*, 30. [CrossRef]
57. Liu, F.; Lin, X.; Yang, G.; Song, M.; Chen, J.; Huang, W. Microstructure and residual stress of laser rapid formed Inconel 718 nickel-base superalloy. *Opt. Laser Technol.* **2011**, *43*, 208–213. [CrossRef]
58. Humphreys, F.J.; Hatherly, M. (Eds.) *Recrystallization and Related Annealing Phenomena*, 2nd ed.; Pergamon: Oxford, UK, 2004.
59. Sun, S.H.; Koizumi, Y.; Saito, T.; Yamanaka, K.; Li, Y.P.; Cui, Y.; Chiba, A. Electron beam additive manufacturing of Inconel 718 alloy rods: Impact of build direction on microstructure and high-temperature tensile properties. *Addit. Manuf.* **2018**, *23*, 457–470. [CrossRef]
60. Dayong, C.; Wenchang, L.; Rongbin, L.; Weihong, Z.; Mei, Y. On the accuracy of the X-ray diffraction quantitative phases analysis method in Inconel 718. *J. Mater. Sci.* **2004**, *39*, 719–721. [CrossRef]
61. Nunes, R.M.; Pereira, D.; Clarke, T.; Hirsch, T.K. Delta phase characterization in inconel 718 alloys through x-ray diffraction. *ISIJ Int.* **2015**, *55*, 2450–2454. [CrossRef]
62. Zinke, M.; Burger, S.; Juettner, S. Properties of Additively Manufactured Deposits of Alloy 718 Using CMT Process Depending on Wire Batch and Shielding Gas. In *Engineering Principles—Welding and Residual Stresses*; IntechOpen: London, UK, 2022; Volume 718, pp. 1–25. [CrossRef]
63. Ola, O.T.; Doern, F.E. A study of cold metal transfer clads in nickel-base INCONEL 718 superalloy. *Mater. Des.* **2014**, *57*, 51–59. [CrossRef]

64. Miao, Z.J.; Shan, A.D.; Wu, Y.B.; Lu, J.; Hu, Y.; Liu, J.L.; Song, H.W. Effects of P and B addition on as-cast microstructure and homogenization parameter of Inconel 718 alloy. *Trans. Nonferr. Met. Soc. China* **2012**, *22*, 318–323. [CrossRef]
65. Lin, Y.C.; Deng, J.; Jiang, Y.Q.; Wen, D.X.; Liu, G. Effects of initial δ phase on hot tensile deformation behaviors and fracture characteristics of a typical Ni-based superalloy. *Mater. Sci. Eng. A* **2014**, *598*, 251–262. [CrossRef]
66. Kindermann, R.M.; Roy, M.J.; Morana, R.; Prangnell, P.B. Process response of Inconel 718 to wire + arc additive manufacturing with cold metal transfer. *Mater. Des.* **2020**, *195*, 109031. [CrossRef]
67. Wu, S.; Peng, H.Z.; Gao, X.; Hodgson, P.D.; Song, H.Y.; Zhu, Y.M.; Tian, Y.; Huang, A.J. Improving creep property of additively manufactured Inconel 718 through specifically-designed post heat treatments. *Mater. Sci. Eng. A* **2022**, *857*, 144047. [CrossRef]
68. Zheng, Y.; Cao, L.; Wang, J.; Xie, J.; Chen, J.; Wang, D.; Wang, S.; Xu, J.; Lu, H. Surface morphology refinement and Laves phase control of plasma arc additively manufactured Inconel 718 via an alternating magnetic field. *Mater. Des.* **2022**, *223*, 111161. [CrossRef]
69. Yu, Z.S.; Zhang, J.X.; Yuan, Y.; Zhou, R.C.; Zhang, H.J.; Wang, H.Z. Microstructural evolution and mechanical properties of Inconel 718 after thermal exposure. *Mater. Sci. Eng. A* **2015**, *634*, 55–63. [CrossRef]
70. Liu, F.; Lyu, F.; Liu, F.; Lin, X.; Huang, C. Laves phase control of inconel 718 superalloy fabricated by laser direct energy deposition via ı aging and solution treatment. *J. Mater. Res. Technol.* **2020**, *9*, 9753–9765. [CrossRef]
71. Neikter, M.; Raja, D.C.; Balachandramurthi, A.R.; Harlin, P. Tailored ductility and strength for enhanced impact toughness of laser powder fusion built Alloy 718. *J. Alloys Compd.* **2021**, *884*, 161374. [CrossRef]
72. Zhao, R.; Zhao, Z.; Bai, P.; Du, W.; Zhang, L.; Qu, H. Effect of Heat Treatment on the Microstructure and Properties of Inconel 718 Alloy Fabricated by Selective Laser Melting. *J. Mater. Eng. Perform.* **2022**, *31*, 353–364. [CrossRef]
73. Hall, E.O. The deformation and ageing of mild steel: III Discussion of results. *Proc. Phys. Soc. Sect. B* **1951**, *64*, 747–753. [CrossRef]
74. Petch, N.J. The ductile-brittle transition in the fracture of α-iron: I. *Philos. Mag.* **1958**, *3*, 1089–1097. [CrossRef]
75. Wang, Y.; Huang, C.; Ma, X.; Zhao, J.; Guo, F.; Fang, X.; Zhu, Y.; Wei, Y. The optimum grain size for strength-ductility combination in metals. *Int. J. Plast.* **2023**, *164*, 103574. [CrossRef]
76. Fayed, E.M.; Brailovski, V.; Jahazi, M.; Medraj, M. Stability of the microstructure and elevated-temperature mechanical properties of additively manufactured Inconel 718 superalloy subjected to long-term in-service thermal cycling. *Mater. Sci. Eng. A* **2022**, *838*, 142790. [CrossRef]
77. Alonso, U.; Veiga, F.; Suárez, A.; Gil Del Val, A. Characterization of Inconel 718® superalloy fabricated by wire Arc Additive Manufacturing: Effect on mechanical properties and machinability. *J. Mater. Res. Technol.* **2021**, *14*, 2665–2676. [CrossRef]
78. Wang, K.; Liu, Y.; Sun, Z.; Lin, J.; Lv, Y.; Xu, B. Microstructural evolution and mechanical properties of Inconel 718 superalloy thin wall fabricated by pulsed plasma arc additive manufacturing. *J. Alloys Compd.* **2020**, *819*, 152936. [CrossRef]
79. Qi, H.; Azer, M.; Ritter, A. Studies of standard heat treatment effects on microstructure and mechanical properties of laser net shape manufactured INCONEL 718. *Metall. Mater. Trans. A Phys. Metall. Mater. Sci.* **2009**, *40*, 2410–2422. [CrossRef]
80. Kuşhan, M.C.; Sofuoğlu, M.A.; Gürgen, S. *Materials, Structures and Manufacturing for Aircraft*; Springer: Cham, Switzerland, 2022; ISBN 978-3-030-91873-6.
81. Radhika, C.; Shanmugam, R.; Ramoni, M.; Bk, G. A review on additive manufacturing for aerospace application. *Mater. Res. Express* **2024**, *11*, 22001. [CrossRef]
82. Rodrigues, T.A.; Duarte, V.; Miranda, R.M.; Santos, T.G.; Oliveira, J.P. Current status and perspectives on wire and arc additive manufacturing (WAAM). *Materials* **2019**, *12*, 1121. [CrossRef]